MNRAS 000, 1–15 (2018) Preprint 14 February 2022 Compiled using MNRAS LATEX style file v3.0

Physical and numerical stability and instability of AGN bubbles in a hot intracluster medium

Go Ogiya[1]★, Pawel Biernacki[2]†, Oliver Hahn[1] and Romain Teyssier[2]
[1] *Laboratoire Lagrange, Université Côte d'Azur, Observatoire de la Côte d'Azur, CNRS, Blvd de l'Observatoire, CS 34229, 06304 Nice, France*
[2] *Center for Theoretical Astrophysics and Cosmology, Institute for Computational Science, University of Zurich, Winterthurerstrasse 190, 8057 Zurich, Switzerland*

arXiv:1802.02177v1 [astro-ph.GA] 6 Feb 2018

Accepted XXX. Received YYY; in original form ZZZ

ABSTRACT

While feedback from Active Galactic Nuclei (AGN) is an important heating source in the centre of galaxy clusters, it is still unclear how the feedback energy is injected into the intracluster medium (ICM) and what role different numerical approaches play. Here, we compare four hydrodynamical schemes in idealized simulations of a rising bubble inflated by AGN feedback in a hot stratified ICM: (traditional) smoothed particle hydrodynamics (TSPH), a pressure flavour of SPH (PSPH), a meshless finite mass (MFM) scheme, as well as an Eulerian code with adaptive mesh refinement. In the absence of magnetic fields, the bubble is Kelvin-Helmholtz unstable on short enough time scales to dissolve it fully in the ICM, which is captured by MFM and RAMSES simulations, while in the TSPH simulation the bubble survives. When the ICM is turbulent, mixing of the bubble with the ICM is accelerated. This occurs if the numerical scheme can capture the instabilities well. The differences in the evolution of the bubble has a surprisingly small influence on the thermal structure of the ICM. However, in the simulations with MFM and RAMSES the bubble disruption leads to turbulent stirring of the ICM which is suppressed in SPH. In the latter the thermal energy remains trapped in the bubble and is transported to large radii. We discuss if the choice of hydrodynamical schemes can lead to systematic differences in the outcomes of cosmological simulations.

Key words: methods: numerical – galaxies: clusters: intracluster medium – hydrodynamics – instabilities – turbulence

1 INTRODUCTION

The heating mechanisms for the gas in the centre of galaxy clusters is important to explain X-ray observations (McNamara & Nulsen 2007; Kravtsov & Borgani 2012; Fabian 2012, and references therein). The cooling timescale of the gas in the centres of galaxy clusters is much shorter than the Hubble time (Fabian & Nulsen 1977; Cowie & Binney 1977; Mathews & Bregman 1978, and many subsequent works), known as the so-called cooling flow problem. If there is no heating source, intra-cluster medium (ICM) would exhibit a strong cooling flow and thus become highly concentrated in the centre of the cluster. This is in contrast with observations of cluster centres, which show that the ratio of the gas mass to the total enclosed mass can be fairly low, ~ 0.01, compared to the cosmic baryon fraction, ~ 0.16. Furthermore, the temperature of the central gas is high, typically $\gtrsim$keV $\sim 10^7$ K (e.g. Lea et al. 1973; Evrard 1997; Pratt et al. 2010; Mantz et al. 2014). These observed properties of the ICM are reviewed by e.g. Fabian (1994) and Fabian (2012, and references therein).

Active Galactic Nuclei (AGN) are promising heating sources to keep the centres of galaxy clusters hot and to prevent gas concentration (McNamara & Nulsen 2007; Kravtsov & Borgani 2012, and references therein). If AGN are powerful enough, the jet power of $P_{\rm jet} \gtrsim 10^{42}$ erg/sec (e.g. Cavagnolo et al. 2010; Nemmen et al. 2012; Godfrey & Shabala 2013), can trigger strong shock waves which compress and heat the ICM (e.g. Sanderson et al. 2005; Sutherland & Bicknell 2007; Mingo et al. 2012; Gaspari et al. 2011; Wagner et al. 2012; Perucho et al. 2014; Lanz et al. 2015). Even if AGN are less powerful, they may induce bubbles of diffuse hot gas. X-ray observations have detected such AGN bubbles as cavities in the ICM (Fabian et al. 2000; McNamara et al. 2001; Gitti et al. 2006; Dong et al. 2010) and in galaxy

★ E-mail: go.ogiya@oca.eu (GO)
† E-mail: biernack@physik.uzh.ch (PB)

© 2018 The Authors

groups and galaxies (e.g. Ohto et al. 2003; Forman et al. 2007; Panagoulia et al. 2014).

Observations have also suggested that significant amounts of the thermal energy might be still captured in hot bubbles (e.g. Bîrzan et al. 2004; Dunn et al. 2005; Shurkin et al. 2008; Sanders et al. 2009). Hence, a theoretical investigation of the interaction between the bubble and the surrounding ambient cluster gas would be of great importance to our understanding of the thermodynamics of the ICM. The rising bubble may also play a role in redistributing heavy elements in the ICM. The processes that govern the rising of the bubble and its subsequent mixing with the surrounding ICM are complex and detailed analytical investigations are difficult. Simplified models have provided valuable insights (e.g. Voit et al. 2017, and references therein), and numerical simulations can provide further insight into the complex processes governing gas in cluster cores.

Numerical simulations of the ICM with AGN feedback can be classified into two types - 1) idealised and 2) cosmological. The former aim to understand the physics by means of idealised setups, which provide full control over the cluster environment and processes. For example, early studies showed that energy and matter redistribution by rising bubbles plays a key role in solving the cooling flow problem (e.g. Churazov et al. 2001; Brüggen & Kaiser 2002). Subsequent simulations with higher resolution and additional physics, including magnetic fields and cosmic rays, demonstrated that the buoyantly rising bubbles redistribute not only energy and mass, but also metals and magnetic fields in the ICM (Reynolds et al. 2005; Sijacki & Springel 2006; Vernaleo & Reynolds 2006; Roediger et al. 2007; Dursi & Pfrommer 2008; Vazza et al. 2010; Guo & Mathews 2011). An interesting insight obtained by magnetohydrodynamic (MHD) simulations is that magnetic tension suppresses mixing instabilities on the bubble surface and thus supports bubbles to rise to larger radii (Robinson et al. 2004; Dong & Stone 2009, see also Biernacki et al., in prep.).

Cosmological simulations provide a more realistic cluster environment and assembly history with turbulence in the ICM driven continuously by both minor and major mergers (e.g. Miniati 2014). Thanks to recent developments in the modelling of supermassive black holes and AGN feedback in cosmological hydrodynamic simulations (e.g. Di Matteo et al. 2005; Kawata & Gibson 2005; Sijacki et al. 2007; Okamoto et al. 2008; Booth & Schaye 2009; Teyssier et al. 2011; Vogelsberger et al. 2013; Steinborn et al. 2015), they have succeeded in reproducing various observational results (Nagai et al. 2007; McCarthy et al. 2010; Di Matteo et al. 2012; Battaglia et al. 2013; Le Brun et al. 2014; Dolag et al. 2016; Dubois et al. 2016; Barnes et al. 2017a,b; Hahn et al. 2017, and refereces therein).

However, full agreement among them has not been achieved yet. The early discrepancy in predicted cluster entropy profiles between Eulerian and Lagrangian methods in non-radiative simulations (Frenk et al. 1999) has been understood as a severe underproduction of entropy in traditional Smooth Particle Hydrodynamics (SPH) methods (e.g. Wadsley et al. 2008; Mitchell et al. 2009; Power et al. 2014). Modern Lagrangian methods solved these shortcomings, but such discrepancies appear in any case less dramatic when optically thin cooling is added and are overshadowed by differences in subgrid models (e.g. Sembolini et al. 2016). However, some suspicion about fundamental differences might still be in order: for example, the central gas mass fraction in the centres of simulated clusters is typically lower than that observed when grid-based hydrodynamical solvers are used in the simulations (Hahn et al. 2017; Barnes et al. 2017a). On the other hand, simulations that adopt SPH claim to reproduce more realistic gas fractions by carefully tuning the AGN feedback model (Battaglia et al. 2013; Le Brun et al. 2014). Similarly, the distribution of metals in galaxy clusters is reproduced in some SPH simulations (Wiersma et al. 2011; Planelles et al. 2014; Rasia et al. 2015). Schaller et al. (2015) found differences in simulations adopting different flavours of SPH when keeping the feedback models fixed, but the differences are small at galaxy cluster masses.

Such discrepancies motivated us to pose the following questions:

- are there issues in AGN feedback modelling?
- do different hydrodynamical solvers agree?
- do the simulations lack the resolution to capture important processes?
- are we missing any of other important non-thermal processes?

Physical viscosity and diffusion are typically negligible in most processes of the formation and evolution of galaxy clusters (e.g. Mo et al. 2010). However, neglecting this physics in numerical simulations may lead the code-dependent numerical, i.e. artificial and physically incorrect, effects which can affect the outcomes of the simulations. Thus we need to give careful attention to this point. Agertz et al. (2007) presented the fundamental differences between SPH and grid based methods with a suite of idealised simulations of a cold dense gas cloud moving through a low-density hot medium. Wadsley et al. (2008) tackled the second question using idealized simulations of a buoyantly unstable and rising hot bubble in an ambient medium. They found that the absence of mixing in traditional SPH schemes leads to an underproduction of entropy compared to grid based codes.

In this paper, we update the findings by Agertz et al. (2007) and Wadsley et al. (2008) using state-of-the-art hydrodynamical solvers that are used in more recent major cosmological simulations. In order to avoid too much complexity, we employ a well-defined, simple setup of a spherically symmetric ICM with a hot bubble inflated by AGN feedback. This setup is similar to the one of Wadsley et al. (2008), but includes self-gravity of the gas, and for which a naïve analytical expectation can be given. In a next step, we introduce a turbulent velocity field to make the model more realistic. We address also the third question by varying the resolution of the simulations. For the first question, we refer readers to Meece et al. (2017) who compared the commonly-adopted sub-grid models of AGN feedback. Regarding the fourth question, our subsequent project will address one of the possibilities - effects of magnetic fields (Biernacki et al., in prep.).

This paper is organized as follows. In Section 2, we describe our simple model of a buoyantly rising bubble inflated by AGN feedback at the centre of a gas sphere of the ICM and also provide the analytical expectation for the fate of the bubble. Section 3 gives a brief description for the numerical codes and methods used in this paper. We describe the setup of our numerical experiments and demonstrate the

results in Section 4. In Section 5, we summarize and discuss the results.

2 INITIAL CONDITIONS AND ANALYTIC EXPECTATIONS

In this section, we set the stage for our model of a stratified hydrostatic medium and describe a hot bubble positioned initially near the centre of our idealised cluster. We present also calculations that demonstrate that such bubbles will buoyantly rise, experience ram pressure and undergo interface instabilities that lead to their ultimate demise by mixing with the ambient medium.

2.1 The ambient medium

We adopt the analytical model proposed by Komatsu & Seljak (2001, hereafter KS01) as a model for the ambient medium. In the analytical model, a gas sphere is embedded in a dark matter (DM) halo with a Navarro-Frenk-White (NFW Navarro et al. 1997) density profile, and the thermal pressure balances with the gravity of the DM halo with a polytropic equation of state while the self-gravity of the gas is neglected. KS01 adopted empirical prescriptions to give the concentration parameter of the halo, $c = r_{100}/r_{\rm s}$, where $r_{\rm s}$ is the scale length of the halo, and the polytropic index, γ, as functions of the virial mass of the DM halo, M_{100}. Here, M_{100} is the mass contained within the virial radius, r_{100}, inside of which, the mean density of the DM halo is 100 times the critical density of the current universe.

Throughout this paper, we adopt a Hubble constant $H_0 = 70.3\,{\rm km/s/Mpc}$ (Komatsu et al. 2011) and we assume $M_{100} = 3\times10^{14}\,{\rm M}_\odot$ and a total gas mass, $M_{\rm gas} = 4.5\times10^{13}\,{\rm M}_\odot$. The concentration parameter of the DM halo and effective polytropic exponent that the analytical model provides are $c = 5.168$ and $\gamma = 1.137$, respectively. The DM halo has a virial radius of $r_{100} = 1.734\,{\rm Mpc}$. The dashed line in Fig. 2 presents the radial profiles of gas density (first row) and temperature (second row) given by this model.

2.2 Equation of motion of a bubble

2.2.1 Buoyancy

Let us consider a hot underdense bubble embedded in a colder stratified ambient gas sphere in hydrostatic equilibrium. If the bubble is displaced from the centre of the ambient gas sphere, it will rise buoyantly if the Schwarzschild condition for convective stability (Schwarzschild 1906),

$$\left|\frac{dT}{dr}\right| < \left|\frac{dT}{dr}\right|_{\rm ad} \tag{1}$$

is *not fulfilled*. Here, r and T are the distance from the centre of the gas sphere and the gas temperature, respectively. The subscript "ad" in the second term indicates the respective relation allowing only adiabatic processes. Treating the bubble as a point mass for simplicity, the acceleration due to buoyancy, $\mathbf{a}_{\rm buo}$, can be written as

$$\mathbf{a}_{\rm buo}(\mathbf{r}) = \frac{\rho_{\rm amb}(r)-\rho_{\rm bub}(r)}{\rho_{\rm bub}(r)}\mathbf{g}(\mathbf{r}), \tag{2}$$

where $\mathbf{r}$ is the position of the bubble relative to the centre, $\mathbf{g}(\mathbf{r})$ the gravitational acceleration at $\mathbf{r}$, and $\rho_{\rm amb}(r)$ and $\rho_{\rm bub}$ indicate the density of the ambient medium at the radius, $r = |\mathbf{r}|$, and of the bubble, respectively. Note that the first term equates with the gradient of the thermal pressure, $-dp/dr$.

2.2.2 Ram Pressure

When the bubble has a non-zero velocity with respect to the ambient medium, it also feels ram pressure. Treating the bubble again as a point mass, the gradient of ram pressure, $\mathbf{a}_{\rm ram}$, is given as

$$\mathbf{a}_{\rm ram}(\mathbf{r}, v) = \frac{v^2}{2\rho_{\rm bub}}\frac{d\rho_{\rm amb}(r)}{dr}\frac{\mathbf{r}}{r}, \tag{3}$$

where v is the relative velocity between the bubble and the ambient medium.

2.2.3 Interface instabilities

As the bubble moves through the ambient medium with non-zero v, we expect the bubble boundary to undergo a Kelvin-Helmholtz instability (KHI, cf. e.g. Landau & Lifshitz 1959) which ultimately will act to dissolve the bubble in the ambient medium. The timescale on which the KHI will act to dissolve the bubble is

$$\tau_{\rm KHI} \sim \frac{\rho_{\rm amb}+\rho_{\rm bub}}{\sqrt{\rho_{\rm amb}\rho_{\rm bub}}}\frac{\lambda}{v}, \tag{4}$$

where λ is the wavelength of the perturbation on the surface of the bubble. The KHI grows exponentially with time, t, i.e., the amplitude of the KHI, $A_{\rm KHI} \propto \exp(t/\tau_{\rm KHI})$.

2.3 Comparison of timescales

Based on our estimates above, the bubble is expected to survive until $\lesssim \tau_{\rm KHI}$ but dissolve after that. Using Eq. (2) and Eq. (3), we can follow the motion of a bubble and estimate the time for the bubble to arrive at r, $\tau(r)$. To make a hot and less dense bubble, the temperature of gas contained within the innermost sphere of a diameter of 20 kpc is set to be 10^9 K, much hotter than the ambient hydrostatic medium (see Fig. 2). Assuming that the heated central sphere itself expands adiabatically behind a rapidly propagating shock (see also Fig. 3) until its pressure balances that of the ambient medium, the diameter of the bubble becomes $\sim 60\,{\rm kpc}$ (with the assumption of adiabatic expansion of the bubble rendering this an upper limit). If the position of the bubble is displaced from the exact centre by some perturbation, it rises buoyantly as long as Eq. (1) is not satisfied.

Fig. 1 compares $\tau(r)$ with $\tau_{\rm KHI}$ and shows that the bubble would be dissolved at $r \gtrsim 200-300\,{\rm kpc}$ where $\tau(r) > \tau_{\rm KHI}$. We compute the bubble density by assuming that the bubble continues to expand adiabatically and use the instant relative velocity between the bubble and the ambient medium at r, $v(r)$, and the wavelength, $\lambda = 59.3\,{\rm kpc}$ to evaluate $\tau_{\rm KHI}$. Since $\tau_{\rm KHI}$ is proportional to the wavelength of the perturbation, this choice of λ would provide the upper limit of the of the KHI-time. Note that we neglect the response of the ambient medium to the motion and expansion of the bubble and assume that its density and temperature stay those of the hydrostatic equilibrium state, for simplicity.

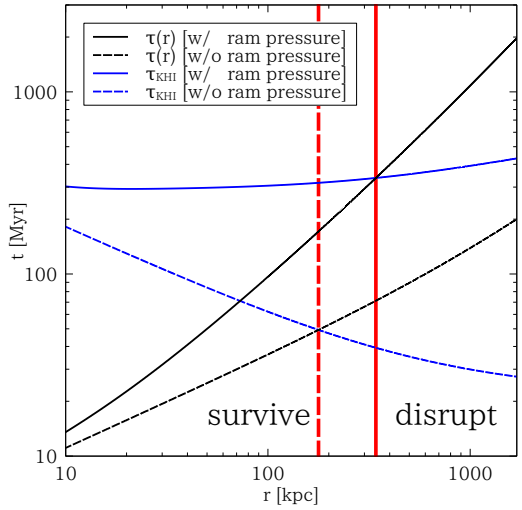

Figure 1. Comparison of timescales. Black lines represent the timescale of the bubble to arrive at r, $\tau(r)$. To estimate the KHI timescale, $\tau_{\rm KHI}$ (blue), the instantanious relative velocity between the bubble and the ambient medium at r, $v(r)$, and the wavelength, $\lambda = 59.3\,{\rm kpc}$ are assumed. For solid (dashed) lines, ram pressure is (is not) taken into account. The bubble is expected to be dissolved at $r \sim 200-300\,{\rm kpc}$ where $\tau(r) > \tau_{\rm KHI}$. Red solid and dashed lines indicate the survival radius of the bubble including and not including ram pressure.

2.4 Introducing turbulence

In contrast to our simplistic model above, the ICM is turbulent (e.g. Schuecker et al. 2004; Hitomi Collaboration et al. 2016, and other observational results) and a substantial amount of turbulent energy may be converted into thermal energy to heat the centre of clusters (e.g. Dennis & Chandran 2005; Zhuravleva et al. 2014; Eckert et al. 2017). In fact, mass estimates of galaxy clusters via the thermal Sunyaev-Zel'dovich effect and assuming hydrostatic equilibrium appear inconsistent with both independent measures of galaxy cluster abundance (cf. Planck Collaboration et al. 2016) and independent mass estimates (Hurier & Angulo 2017), pointing possibly to a much larger contribution of non-thermal pressure than what is commonly found in simulations (see also e.g. Lau et al. 2009; Nelson et al. 2014).

Here, we introduce turbulence in order to quantify the additional effect it can have on the mixing of rising AGN bubbles in purely hydrostatic simulations, as well as the opposite effect, how the bubble can drive turbulence itself. We adopt a simple model in which we sample an isotropic Gaussian Kolmogorov velocity spectrum (e.g. Landau & Lifshitz 1959), for which

$$\left\langle \tilde{\mathbf{v}}(\mathbf{k}) \cdot \tilde{\mathbf{v}}^*(\mathbf{k}') \right\rangle \propto |k|^{-11/3} \delta_D(\mathbf{k}-\mathbf{k}'), \quad (5)$$

where a tilde indicates a Fourier transformed field. An arbitrary velocity field can be decomposed into longitudinal and transversal modes, with the respective scalar potential ϕ_ν and the vector potential $\mathbf{A}_\nu$, so that

$$\mathbf{v} = \boldsymbol{\nabla}\phi_\nu + \boldsymbol{\nabla} \times \mathbf{A}_\nu. \quad (6)$$

We assume here that the potentials are being given through multiplication of a random scalar field $G\{0,1\}$ and an independent random vector field $\mathbf{G}\{0,1\}$ (both of which are assumed to be fields of Gaussian white noise with zero mean and unit variance) with the square-root of the spectrum, so that in Fourier space

$$\tilde{\phi}_\nu(\mathbf{k}) = \alpha\phi_0\, k^{-17/6}\, \tilde{G}\{0,1\}, \quad \tilde{\mathbf{A}}_\nu(\mathbf{k}) = \beta\phi_0\, k^{-17/6}\, \tilde{\mathbf{G}}\{0,1\}. \quad (7)$$

Here, ϕ_0 is a normalisation constant, and the parameters α and β can be used to adjust the relative importance of longitudinal and transversal velocity modes ($\alpha^2+\beta^2=1$ to maintain normalisation and we set $\alpha^2=\beta^2=0.5$). Note that the Kolmogorov spectrum typically holds only between the driving scale and the dissipation scale. In our model, we set the driving scale k_0 by hand and zero all modes with $k < k_0$ where $k_0 = 2\pi/(r_{100}/4)$ in this paper, while we assume that the dissipation scale is unresolved. In practice, we create a random realisation of a velocity field on a mesh of resolution $N_{\rm v}^3$, with $N_{\rm v} = 256$. The finite resolution automatically introduces a small-scale cut off of $2\pi/(r_{100}/128)$, and we assume that the one-point variance on the grid, $\sigma_{\rm v}^2$ can be equated to a non-thermal temperature of $T_{\rm nt}$. For the simulation codes used in this study, we add the respective velocity by interpolating from the particle/AMR cell positions to the grid on which we made a realisation of the velocity field. Then the corresponding thermal energy of $k_{\rm B}T_{\rm nt}$, is subtracted from each particle/AMR cell. This keeps the total energy of the system constant down to the level of Poisson noise in the grid and particle distribution.

3 METHODS

In order to compare theoretical expectations outlined in the previous section with full non-linear calculations, we run idealized hydrodynamical simulations of self-gravitating gas using two independently developed numerical codes. This section gives a brief description of these codes and the methods they adopt to solve the equations of ideal hydrodynamics.

3.1 Initial conditions

As a model for the hot cluster gas, we adopt the model of Komatsu & Seljak (2001) that we already described in Subsection 2.1. In our numerical experiments, we however make two important modifications compared to this model: First, we include the self-gravity of the gas sphere, which was ignored in the KS01 model. To this end, we rescale the gravitational acceleration of the model to that of only the dark matter by multiplying with a factor of $(1 - M_{\rm gas}/M_{100})$ and calculate the self-gravity of the gas self-consistently. Second, we adopt a polytropic exponent of $\gamma = 5/3$, while KS01 originally adopted the effective polytropic index that they derived as a constraint of the model ($\gamma = 1.137$ for our cluster parameters).

As a model for the bubble inflated by a central AGN, we use a sphere of radius 10 kpc placed close to the centre of the halo and heated to a temperature of $10^9\,{\rm K}$. The associated thermal energy, $\sim 3\times10^{59}\,{\rm erg}$, is identical in all experiments and roughly consistent with what observations suggest (e.g. Bîrzan et al. 2004).

3.2 Lagrangian methods

For all Lagrangian hydrodynamic simulations, we use the GIZMO code[1] (Hopkins 2015), which includes various Lagrangian methods, among them TSPH, PSPH and MFM, that we use in what follows.

- Traditional SPH (TSPH; e.g. Lucy 1977; Gingold & Monaghan 1977; Monaghan 1992) has been widely used in astrophysics, especially to study structure formation in the universe (for recent reviews e.g. Rosswog 2009; Springel 2010a; Monaghan 2012; Price 2012, and references therein) because of its great advantages, e.g. Galilean invariance, automatically adopted spatial resolution and exact mass conservation. However, it is also known that TSPH has difficulties to deal with fluid mixing. For example, the artificial tension on the contact surface of multi-phase fluids suppresses the growth of the KHI (e.g. Okamoto et al. 2003; Agertz et al. 2007).
- Subsequent studies have made a lot of efforts to overcome the difficulties (e.g. Ritchie & Thomas 2001; Inutsuka 2002; Read et al. 2010; Abel 2011). One of the modern formulations of SPH, the pressure flavour of SPH (PSPH; Saitoh & Makino 2013; Hopkins 2013) resolved them by replacing the volume element estimated from the mass density of an SPH particle (which is a technique used in TSPH) with that estimated from pressure (or energy density) of the particle and handled the fluid mixing instabilities, including the KHI and Rayleigh-Taylor instability.
- Hopkins (2015) recently proposed a new class of particle methods for numerical hydrodynamics, meshless finite mass (MFM) and meshless finite volume (MFV), which have advantages of both SPH and grid-based schemes. These methods adopt a kernel-weighted volume discretization like SPH, but with a high-order matrix gradient estimator. A Riemann solver evaluates fluid (mass, momentum and energy) fluxes between particles, whose effective volume elements are overlapped. The limit of the MFM/MFV method with an infinitely sharply peaked kernel function corresponds to the moving-mesh method with non-regular deformed grids, e.g. the Voronoi tessellation (Springel 2010b; Duffell & MacFadyen 2011; Gaburov et al. 2012).

The initial particle distribution which follows the KS01 density profile is drawn by using the rejection sampling scheme and thermal energy is assigned to each particle by interpolating the temperature profile of the KS01 model. To model AGN bubbles in the ICM, we increase the thermal energy of particles contained in the bubble within a radius of 10 kpc to have temperature of 10^9 K. In all runs using GIZMO, we set the smoothing length, h, to the equivalent of what contains 32 neighbour particles and use the cubic spline kernel function. The gravitational softening in computing the gas self-gravity is fixed to be 1 kpc. We employ 67 108 864 particles, unless stated otherwise. The maximum spatial resolution is typically $2h \sim 10$ kpc at the centre and the mass resolution is $6.7 \times 10^5\,\mathrm{M}_\odot$. The self-gravity of the gas is computed using the tree algorithm (Barnes & Hut 1986) with an opening angle of $\theta = 0.7$ (default setting in GIZMO). The gravity of the DM halo is computed with a fixed analytical potential (see Subsection 2.1 and Subsection 3.1 for details).

[1] publicly available at `https://bitbucket.org/phopkins/gizmo/wiki/Home`

3.3 Eulerian methods

For the Eulerian hydrodynamics simulations, we use the adaptive mesh-refinement (AMR) code RAMSES[2]. RAMSES solves the hydrodynamic equations using a second-order, unsplit Godunov scheme. This method is known to accurately capture shocks. Fluxes are reconstructed from the cell-centred values with the Harten-Lax-van Leer-Contact (HLLC) Riemann solver that uses a first-order MinMod Total Variation Diminishing scheme. RAMSES uses a tree structure, which allows for cell-by-cell refinement, thanks to which computational resources can be focused at high-density regions.

The initial conditions for the density and pressure of the ICM sphere are interpolated from the respective KS01 profiles. The AGN bubble is modelled by raising the temperature of all cells whose centres fall within the bubble radius to 10^9 K. We have used boundary conditions which allow only for outflow. Cells are refined based on the quasi-Lagrangian approach, when gas mass in the cell exceeds $1.94 \times 10^7\,\mathrm{M}_\odot$. This leads to a similar number of leaf cells, 59 211 888 at the initial time, compared to the number of particles in GIZMO runs. Maximum spatial resolution achieved is 1.64 kpc (11 levels of refinement), while minimum resolution is 52.5 kpc (6 levels of refinement; base grid). We use analytical gravity for the DM halo described in Subsection 2.1 and Subsection 3.1. Self-gravity of the gas is calculated using the relaxation solver in RAMSES and added to the halo potential.

3.4 Spherical 1D validation code

For spherically symmetric initial conditions in general cases where analytic solutions do not exist, we have run a simple spherical 1D MUSCL solver which includes solvers for one-dimensional spherical hydrodynamics and self-gravity. We use this 1D code in order to validate the solutions of the three-dimensional solvers discussed above during those stages when the solution is still close to spherically symmetric. The initial gas density and temperature are set as in RAMSES. The boundary conditions are reflective in the centre and outflow at the outer boundary. Self gravity can be calculated trivially in spherical 1D by summing mass shells up to a given radius and the same analytical potential with that in runs of GIZMO and RAMSES is adopted to compute the gravity of the DM halo. A more detailed description and tests for the 1D code can be found in Subsection A2.

4 SIMULATIONS

In what follows, we present the results of our numerical experiments. We first verify that our ICM is indeed close to hydrostatic equilibrium and remain so over an extended period of time with all numerical methods. Next, we investigate the evolution of an AGN-inflated hot bubble in such a hydrostatic ICM. We also consider the sophistication of

[2] publicly available at `https://bitbucket.org/rteyssie/ramses`

our ICM model by replacing a fraction of its thermal energy with turbulence.

4.1 Stability of the ambient gas sphere

We first verify how close to hydrostatic equilibrium the clusters remain over an evolution time of 1 Gyr. The results of this stability test are shown as solid lines in Fig. 2. Despite the differences from the original model of KS01 (self-gravity of the gas and equation of state), the differences between the original model (brown dashed line) and the simulation results are small. The gas profiles for density (first row) and temperature (second row) show a very minor evolution due to the system readjusting to a new hydrostatic equilibrium with an expansion of ~ 30km/s. More remarkably, a similar degree of stability is seen when we replace some thermal energy with turbulent kinetic energy. And, even if we include turbulence at a very high level of $T_{\rm nt} = 0.5T_{\rm vir}$ in the ambient gas sphere, the spherically averaged radial profiles of density and temperature do not significantly deviate from the state shown in Fig. 2. Here $T_{\rm vir}$ is the virial temperature of the DM halo, $T_{\rm vir} \approx 1.8 \times 10^7$ K and the corresponding velocity dispersion is $\sigma_{\rm vir} \sim 835$ km/s. We can therefore conclude that the gas sphere is reasonably stable and we adopt it as the ambient ICM of the AGN bubble in the following simulations. We note that our decision to neglect radiative cooling throughout this paper is well justified since the cooling timescale is longer than the buoyant timescale (~ 1 Gyr), that we study here, by a factor of ~ 5, as shown in the fourth row.

In all cases we investigated, the turbulent energy decayed in a much shorter time, ~ 30Myr, than the total time of evolution of 1 Gyr. We also note that the Poisson particle noise puts the gas locally out of hydrostatic equilibrium in all runs using GIZMO . This drives a persistent 'particle jitter' since the system responds by producing velocity dispersion (third row) which carries the difference in internal energy when compared to RAMSES and the 1D code.

4.2 Expansion of a central AGN bubble

In this subsection, we study the expansion of an AGN bubble inflated at the centre of the ICM sphere. We increase the initial temperature of fluid elements, i.e. particles in the GIZMO runs and cells in RAMSES and the 1D code, within a central spherical region of 10 kpc to 10^9 K while the density profile follows that of the KS01 model. The initial gas velocity is set to zero, i.e. we do not include turbulent velocities yet. While the central bubble is buoyantly unstable according to the Schwarzschild stability condition for convection, Eq. (1), the instability should not arise due to the symmetry of the system. In perfect symmetry it should just expand, but particle noise (GIZMO) and anisotropy due to the Cartesian mesh (RAMSES) break this symmetry and let the bubble rise after some time (see Appendix B). During the early phase of the simulations the bubble remains however symmetric and we can compare the results of the 3D simulations with that of 1D simulations with a much higher resolution.

Fig. 3 depicts radial profiles of gas density (upper), temperature (middle) and radial velocity (bottom) after

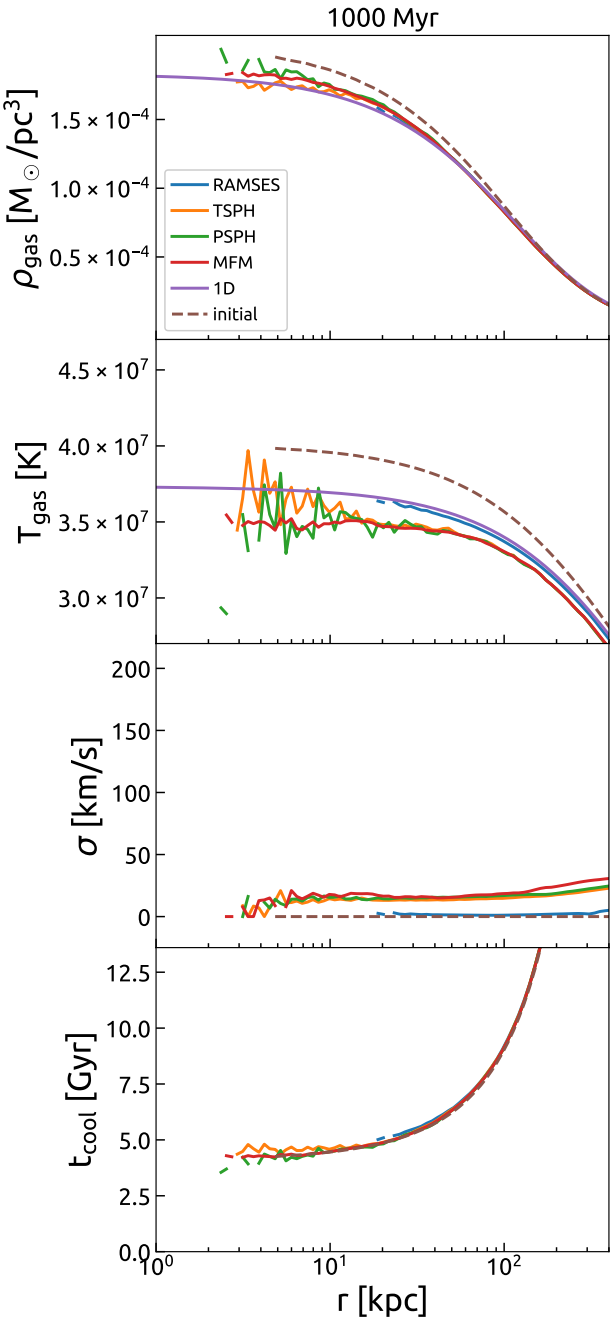

Figure 2. Radial profiles of gas density (first panel), temperature (second), velocity dispersion (third) and cooling timescale (fourth) after 1 Gyr of isolated evolution. Solid lines show profiles from numerical simulations using RAMSES(blue), TPSH (yellow), PSPH (green), MFM (red) and the 1D code (purple), and the brown dashed one represents the profiles of the KS01 model. Each simulation is initialised in the same way - density and temperature follow KS01. All runs are performed at a lower resolution than in the runs with an AGN bubble - GIZMO simulations with 8 388 608 particles, RAMSES simulation with `levelmax`=9.

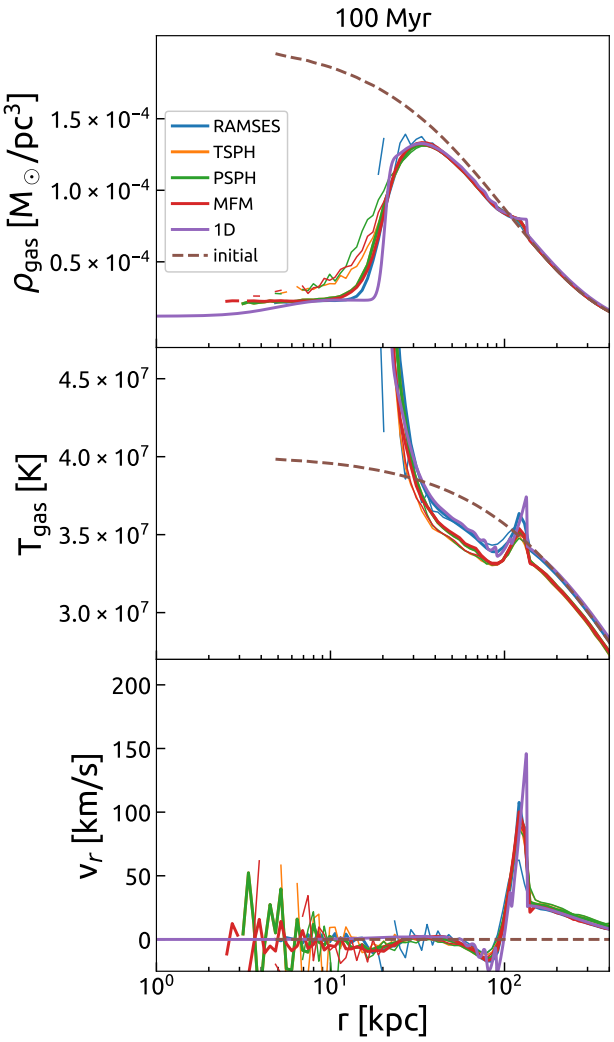

Figure 3. Radial profiles of gas density (upper), temperature (middle) and radial velocity (bottom) 100 Myr after an injection of thermal energy by raising the temperature in the central 10 kpc to 10^9 K. Solid lines show profiles from numerical simulations using RAMSES(blue), TSPH (yellow), PSPH (green), MFM (red) and the 1D code (purple). Thick and thin lines are the results of simulations with the high- (64 million particles in the GIZMO runs and `levelmax`=11 in the RAMSES run) and low resolution (8 million particles in the GIZMO runs and `levelmax`=9 in the RAMSES run), respectively. The initial condition is shown as a brown dashed line.

100 Myr. The expanding bubble creates a strong shock wave which propagates outward. The shock positions in the simulations with different hydrodynamic solvers agree very well with each other (~ 100 kpc). The shock wave leaves a diffuse and hot core at the centre by compressing and accumulating the ambient ICM. While the overall features of the 1D solution are captured by all 3D runs, some differences in the core ($r \lesssim 10$ kpc) are visible due to the lack of resolution in the 3D runs. The profiles obtained in 3D simulations are consistent with each other in the radial range of $r = 10^1 - 10^3$ kpc. Comparing the results of 3D simulations at high (thick lines) and low (thin lines) resolution, the profiles are numerically converged down to $r \sim 20$ kpc, which corresponds to the spatial resolution in the simulations with lower resolution. An additional interesting difference between the 1D and 3D runs is the presence of a pulsating mode in the 1D run interior to the shock and visible as wiggles behind the shock position. It appears that due to lack of resolution such modes are efficiently damped out in the 3D runs.

4.3 A rising bubble in non-turbulent ICM

In this subsection, we investigate the rising of buoyantly unstable AGN bubbles and their interaction with the ambient ICM. As in the simulations of the previous section, we change the initial setup by increasing the temperature of fluid elements within the bubble with a radius of 10 kpc to 10^9 K. Now however, the centre of the bubble is shifted to the upper right oblique 45 degree direction in the $x-y$ plane by 10 kpc from the centre, keeping the temperature outside the bubble and density to be those of the KS01 model. Turbulence is not taken into account and the initial velocity is set to be zero. Since the shifted hot bubble breaks both the Schwarzschild stability condition for convection, Eq. (1), and the symmetry of the system, it must be buoyantly unstable and rising. The amount of the injected thermal energy is almost the same as that in the simulations with a *central* bubble, $\sim 3 \times 10^{59}$ erg.

Fig. 4 shows slices of gas density after 1 Gyr in the runs with the shifted bubble. The fate of rising bubbles very clearly depends strongly on the choice of hydrodynamical solvers. The bubble is rising towards the direction of the initial displacement (upper right oblique 45 degree direction in the $x-y$ plane). It survives unharmed and reaches large radii in the TSPH run (upper left). This result is inconsistent with the analytical expectation discussed in Fig. 1 and caused by the well-known suppression of fluid instabilities by the spurious surface tension (e.g. Okamoto et al. 2003; Agertz et al. 2007). In other runs, the bubble is dissolved by the KHI while configurations are different from one another. The bubble is fragmented into smaller ones in the PSPH run (upper right). In contrast, the MFM one (lower left) looks very similar to the RAMSES result (lower right), while the symmetry of the structure is broken in the MFM run by Poisson noise contained in the initial particle distribution (see also Appendix C for a discussion of resolution effects). The difference in bubble morphology between hydrodynamical solvers of translates of course directly into differences in the redistribution of mass, including metals, and energy by the rising bubble.

In order to better visualize the fate of the heated fluid elements, we next study how the rising bubble is dissolved in the ICM in more detail by explicitly tracking the fluid elements initially contained in the heated sphere. For the GIZMO runs (TSPH, PSPH and MFM), the Lagrangian nature allows us to follow the heated fluid elements through the ID of particles. If metal mixing is not explicitly performed in SPH, this would also track the evolution of metals contained in the hot bubble. While MFM method computes the fluxes between particles like Eulerian schemes and thus gas initially contained in the bubble may dissipate, we use the ID of particles to follow the heated fluid elements. In Eulerian schemes, like RAMSES, tracking fluid elements is more complicated. We take a simple approach here and follow the gas that was initially within the bubble by injecting a pas-

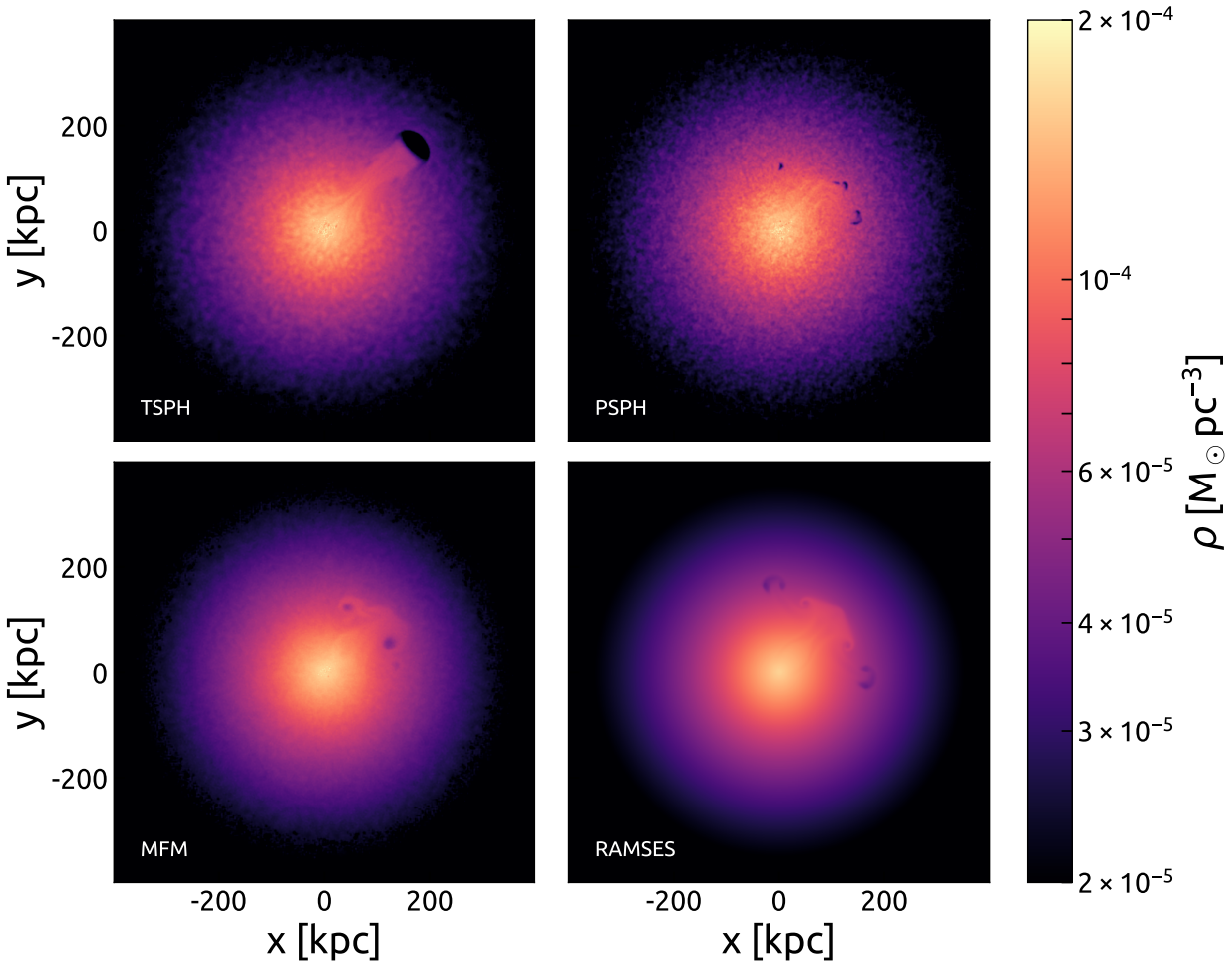

Figure 4. Slices through the gas density distribution for TSPH (top left), PSPH (top right), MFM (bottom left) and RAMSES (bottom right) after 1 Gyr of evolution of a bubble initially shifted from the centre. Each simulation is initialised in the same way - density and temperature follow KS01 and we artificially raise the temperature within the bubble whose centre is shifted to the upper right oblique 45 degree direction in the $x-y$ plane by 10 kpc from the centre of the gas sphere to 10^9 K. The radius of the bubble, 10 kpc, is the same as the runs shown in the previous section.

sive tracer variable in the grid, which is advected with the flow of the gas. This is similar in spirit to injecting metals from supernovae explosions, but in our case we inject the tracer only at the beginning of the simulation and its value in no way modifies any other properties of the grid. This method only approximates tracking of the gas flow in the grid and a more advanced method which uses tracer particles in RAMSES is currently in development (Cadiou et al., private communication). Having that in mind we caution that direct comparison between grid passive tracer and particle IDs can be only qualitative. On the other hand, both cases in fact correspond rather well to the evolution of metals in the flow in the different methods.

Fig. 5 shows the projected density, integrated along the line of sight (LoS), of gas initially contained in the heated bubble at 1 Gyr. It is apparent that, in all cases, the bubble is not fully mixed with the ICM yet, while the specific bubble configuration depends on the choice of hydrodynamical solver, just like the density distribution of the ICM. In the TSPH run (upper left), the heated fluid elements are confined to a small region which corresponds to the less-dense cavity in the upper left panel in Fig. 4. This is another indication that the bubble survives largely unaffected in the TSPH run due to the artificial suppression of the growth of fluid instabilities. In other runs, the bubble is more elongated and less-dense compared with the TSPH run since they handle the instabilities better while the bubble is not completely dissolved and mixed with the ICM even in these runs. In the PSPH (upper right) and MFM (lower left) runs, one can find small density fluctuations on the bubble surface which originate from the Poisson noise in drawing of the initial particle distribution. The bubble has a symmetric structure in the RAMSES run thanks to the absence of such noise. Fluctuations in density and velocity fields would of course always exist in the real ICM. We will study the impact of such 'noises' below in Subsection 4.4 by introducing, in a controlled way, a turbulent velocity field.

The pressing question is of course whether such mor-

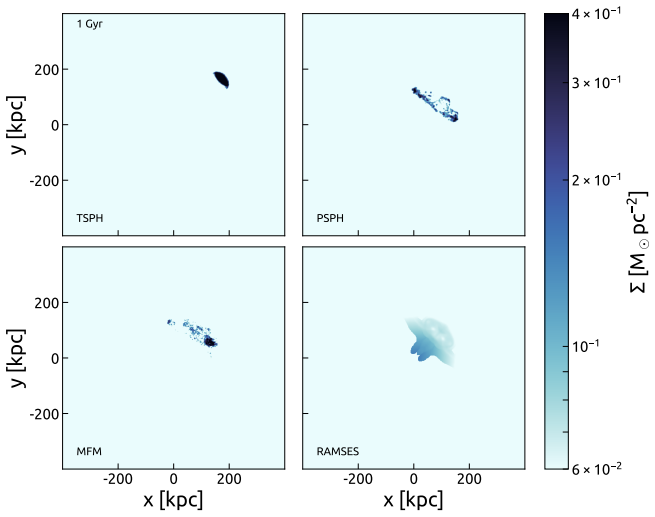

Figure 5. Projection of the density distribution of gas initially contained in the heated bubble for TSPH (top left), PSPH (top right), MFM (bottom left) and RAMSES (bottom right) after 1 Gyr of evolution. The same simulations as in Fig. 4 are shown.

phological differences are also reflected in integral properties of the ICM and thus affect the efficiency of AGN feedback. We thus next investigate how the bubble redistributes mass and energy into the ICM in Fig. 6. The evolution of the profiles obtained from the quarter of the box in which the bubble rises is drawn from the left-most to right-most columns. As shown in Fig. 3, the blast wave ignited by the injected thermal energy reaches to $r \gtrsim 100$ kpc at $t = 100$ Myr. In those runs the energy was damped at the centre of the gas sphere. Assuming the self-similarity of the Sedov-Taylor solution and that the blast wave expands analogously in the runs in which the bubble is shifted, then it would reach $r = 200 - 300$ kpc at $t = 300$ Myr. Indeed, as expected, it appears as peaks in the outskirts ($r \sim 300$ kpc) in the profiles of temperature (second row) and velocity dispersion (fourth row) of the left-most column. At later times it passes through the radial range demonstrated in Fig. 6. Hence the dominating peaks shown in this figure are not originated by the blast wave, but by the rising bubble.

The bubble appears as the bump in the density profile (first row) and as peaks in others. Remarkably, we do not observe significant differences in the density profile. As illustrated in Fig. 4, the hot bubble robustly survives for a long time in the TSPH run because of the spurious tension and we see rising of the hot bubble in the profiles of temperature (second row) and entropy (third row). On the other hand, because the bubble is being dissolved and turbulent motions could arise in MFM and RAMSES runs, the thermal energy contained in the bubble is converted into kinetic energy (fourth row) and the peaks are less pronounced in the profiles of temperature and entropy. The behaviour of the PSPH run is intermediate between the two groups, as expected from Fig. 4 in which the bubble is fragmented into smaller ones in the PSPH run. Note the velocity dispersion, 100-200 km/s, of the turbulent motion driven by the bubble is roughly consistent with the observation of the Perseus cluster (Hitomi Collaboration et al. 2016) and simulation results by Lau et al. (2017, but see also Reynolds et al. 2015).

In summary, the choice of hydrodynamical solver does change the fate of the buoyantly unstable hot bubble and the mass and energy redistribution driven by it in simulations. In the TSPH run, the rising bubble survives for a time inconsistent with the analytical expectation and reaches large radii because spurious tension suppresses the growth of fluid instabilities on the surface. As a result, the thermal energy is locked in the bubble and a smaller fraction of energy, compared with those in the runs using the other hydrodynamical solvers, is distributed to the ambient medium. On the other hand, in the simulations using hydrodynamical solvers which can handle fluid instabilities, the bubble is dissolved in a timescale consistent with the analytical expectation (a few 100 Myr, see Fig. 1) and the thermal energy originally contained in the bubble is converted to non-thermal turbulent energy. In the real ICM, energy would continuously change the form, e.g. transformation from thermal energy to kinetic energy (via bubble rising) and vice versa (via dissipation).

In addition, the different evolution of the bubble can also lead to differences in the metal distribution in the ICM. Supposing that the bubble, which comes from the centre of the cluster, is metal enriched (if metallicity gradients are present), a more diffusive metal distribution, i.e. lower metallicity, would be observed in simulations using the schemes which can handle fluid instabilities (see e.g. Martizzi et al. 2016). This would be further enhanced if the metals are diffused between fluid elements. We study the more complicated and realistic phenomena, rising of an AGN bubble in a turbulent ICM, in the next section.

4.4 A rising bubble in a turbulent ICM

This subsection investigates how small fluctuations in the ICM affect the rising bubble and also their back-reaction. In order to study this effect, we introduce a turbulent velocity field following a Kolmogorov power spectrum (see Subsection 2.4) with the non-thermal temperature of $T_{\rm nt} = 0.03 T_{\rm vir} \approx 5.4 \times 10^5$K which corresponds to a velocity dispersion of 147km/s, consistent with the X-ray observation of the Perseus cluster (Hitomi Collaboration et al. 2016, see also ZuHone et al. 2017). In the initial conditions of the ICM we subtract the corresponding thermal energy from the ICM. Other parameters such as resolution parameters, bubble temperature and size, are the same as those in Subsection 4.3.

Fig. 7 shows the projected density distribution of gas initially contained in the heated bubble at 1 Gyr in the runs with the turbulent velocity field. Because of the perturbations due to turbulence, the bubble does not rise in the direction of the initial offset (upper right oblique 45 degree direction in the $x-y$ plane). In addition, turbulence introduces perturbations of smaller wavelengths which grow faster (see Eq. (4)) and thus enhances instability of the bubble surface. As a result, the bubble is more quickly disrupted and mixed with the ICM compared to the non-turbulent case (Fig. 5), using hydrodynamical schemes which can handle the instabilities (PSPH, MFM and RAMSES). However, just as in the non-turbulent run, the bubble in the TSPH run robustly survives due to the suppression of the growth of fluid instabilities by artificial surface tension (upper left). Note that

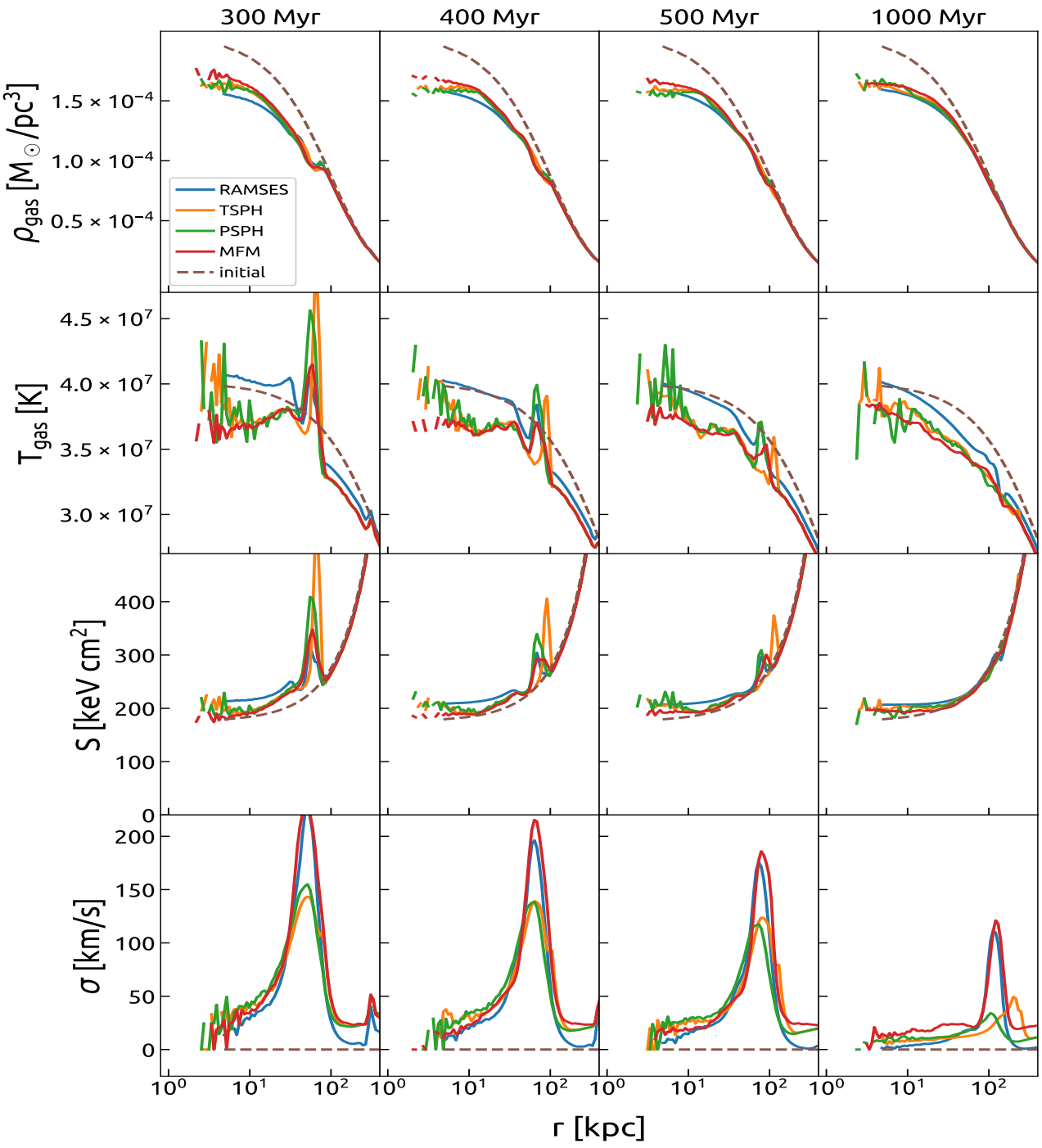

Figure 6. Mass-weighted profiles after evolution of 300 Myr (first column), 400 Myr (second), 500 Myr (third) and 1 Gyr (fourth). We focus our analysis only on the quarter of the box in which the bubble evolves. The profiles of gas density (first row), temperature (second), entropy (third) and three-dimensional velocity dispersion (fourth) are shown. Solid lines show profiles from numerical simulations using RAMSES (blue), TPSH (yellow), PSPH (green) and MFM (red). The brown dashed line represents the KS01 model.

the distance from the centre of the cluster to the (remnants of) bubbles in the turbulent runs is smaller than those in the non-turbulent ones. This and enhanced mixing imply that redistribution of mass, including metals, and energy may be also enhanced around the centre in this case.

We study this point using Fig. 8 which presents the profiles of gas density (first row), temperature (second), entropy (third) and velocity dispersion (fourth). The evolution is shown from the left-most to right-most columns. Unlike before, we now use the whole simulation box to measure the profiles since the direction of rising of the bubble is no longer the same in all runs, as shown in Fig. 7. We note that this

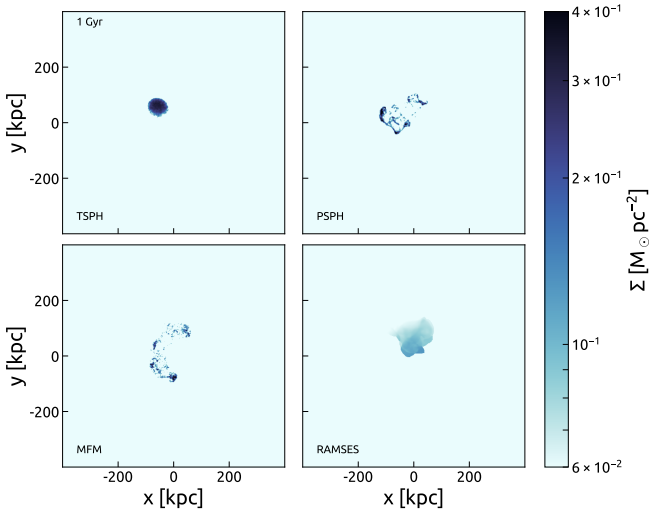

Figure 7. Projection of the density distribution of gas initially contained in the heated bubble for TSPH (top left), PSPH (top right), MFM (bottom left) and RAMSES (bottom right) after 1 Gyr of evolution. Here, the results of simulations with a controlled turbulent velocity field of $T_{\rm nt} = 5.4 \times 10^5$ K are shown.

dilutes the signature of bubbles in the profiles since the part of the simulation box that is not significantly affected by the bubble is included in the analysis. We see no significant differences between hydrodynamical solvers in the first three profiles from the top. However, peaks in the velocity dispersion profiles are more evident in the MFM and RAMSES runs compared with the SPH runs. Again, we interpret this as differences in the efficiency of conversion of thermal energy to turbulent (kinetic) energy when the bubble rises.

It is also worth mentioning that the turbulence decays in all runs, especially in the centre of the cluster where the crossing time is shorter than that measured at the outskirts. Interestingly, the decay of the turbulent velocity field is more significant in the SPH runs compared with the MFM and RAMSES ones. Since perturbations with shorter wavelength, which are introduced by turbulence and grow faster, enhance dissolving of the bubble and mixing with the ICM, these mechanisms would be non-linearly degraded in SPH simulations, while a stronger turbulent velocity field is kept in the MFM and RAMSES runs. We expect that the sub-grid physics models in cosmological simulations which trigger sequential and/or multiple AGN bubbles in the ICM can enhance such contrasts between hydrodynamical solvers. To test this hypothesis, more systematic comparison studies varying not only hydrodynamical solvers but also resolution and sub-grid physics would be needed, which is however beyond the scope of this brief study.

5 SUMMARY AND DISCUSSION

AGN feedback is believed to be an important heating source to keep the ICM in the cluster centre hot and diffuse, and a key to avoid the central cooling flow problem. A number of studies have used numerical simulations to investigate the effect of AGN feedback on the properties of the ICM. However, despite progress in hydrodynamical solvers and modelling of AGN feedback in numerical simulations, a full consensus among cosmological hydrodynamical simulations has not been reached yet and simulations for cluster cosmology are not yet predictive. This situation motivated us to investigate one of the possible reasons for the inconsistency: the difference in the hydrodynamical schemes employed in various simulations. For this purpose, we studied the evolution of rising bubbles inflated by AGN feedback in ideal self-gravitating hydrodynamics. According to observations, the bubbles may be pockets of a significant amount of thermal energy (and cosmic rays, which are however not yet routinely included in cosmological simulations) and hence studying the interaction between the bubble and the ICM is important to make progress.

Using a simplified model, we first showed that a hot bubble will rise buoyantly in the ICM and is prone to surface instabilities that act to disrupt and mix it over time scales of 1 Gyr for a typical cluster of a few $10^{14}\,{\rm M}_\odot$. If the hydrodynamical solver captures fluid instabilities (i.e. the KHI here) well (such as MFM and RAMSES that we studied here), the bubble is disrupted as expected. However, the bubble survives for a longer time than the analytical expectation in simulations using traditional SPH due to spurious surface tension suppressing the growth of instabilities. In the simulation employing the PSPH scheme, we observed that the bubble instead fragments into smaller ones. In addition, we found that if the bubble is metal enriched compared to the ICM at larger radii, a more diffusive metal distribution, i.e. lower metallicity, may be observed in simulated galaxy clusters using hydrodynamical solvers which can model well fluid instabilities (see also e.g. Martizzi et al. 2016), and particularly so in when comparing with Lagrangian schemes that in addition neglect metal diffusion at the fluid element scale.

Because of the difference in bubble mixing, the energy redistribution in the ICM driven by the rising bubble depends somewhat, but less than initially expected, on the choice of hydrodynamical solvers in simulations. Using the hydrodynamical solvers that can capture fluid instabilities, the thermal energy contained in the bubble is transformed more readily into kinetic energy because dissolving of the bubble drives turbulent motion in the ICM. In contrast, the thermal energy is captured in the surviving bubble and transported to large radii in the TSPH simulation. The energy redistribution observed in the PSPH simulation is similar to that in the TSPH run.

In a second step, we investigated whether the various methods agree better in a turbulent ICM, where random motion act to increase bubble disruption and mixing. When the numerical method resolves well fluid instabilities (here MFM and RAMSES), the thermal energy initially contained in the hot bubble is again efficiently converted to kinetic energy of the turbulent motion. More surprisingly, even if we include the turbulent velocity field, the bubble robustly survived in the TSPH simulation while it is more significantly dissolved and mixed with the ICM in all other hydrodynamical solvers. We also found that in general the SPH schemes used in this study damp the turbulent velocity field more strongly than both RAMSES and MFM. And, they also lead to less efficient conversion of the hot bubble to turbulent motion.

In summary, we have observed significant differences in

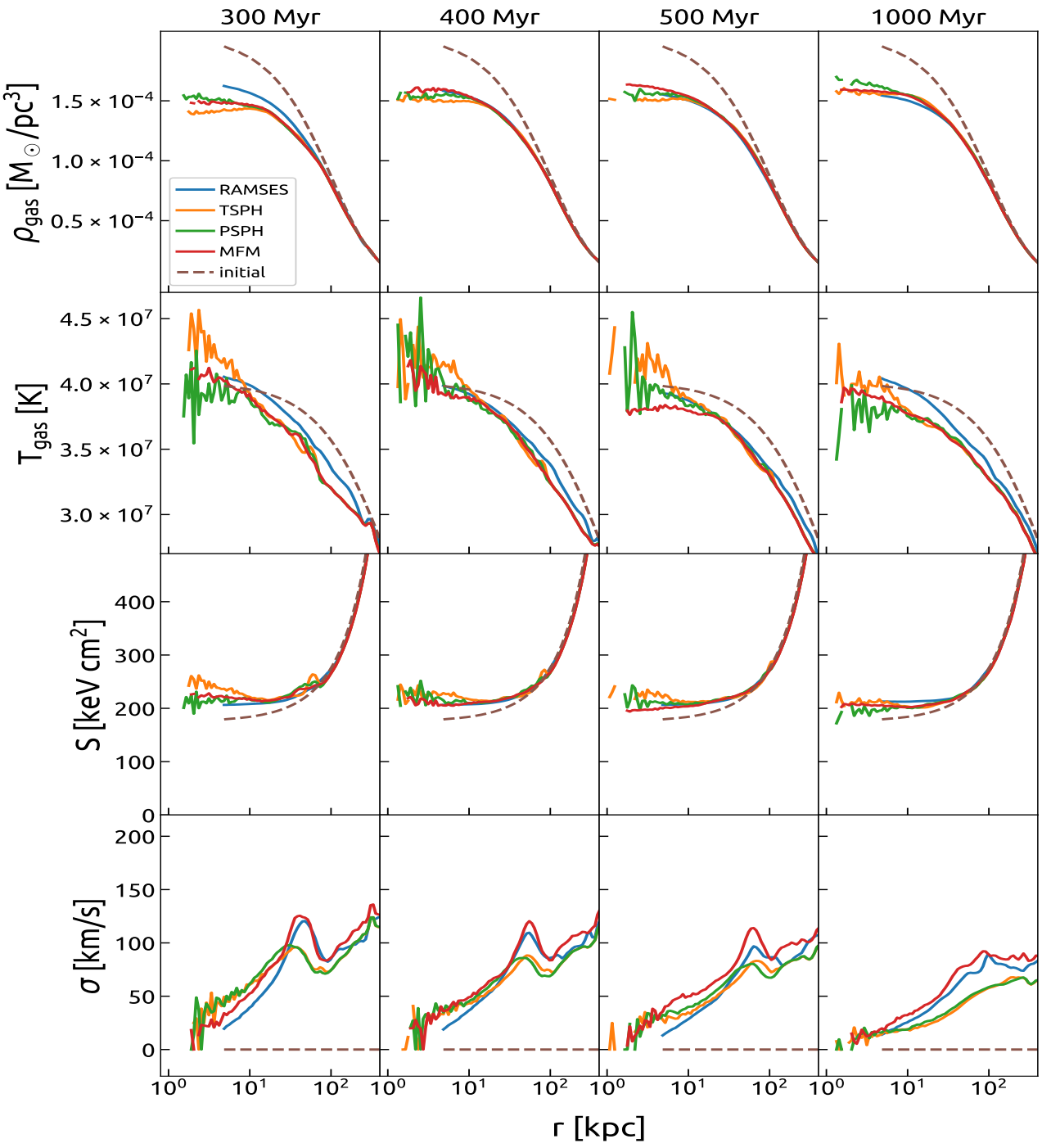

Figure 8. Mass-weighted profiles after 300 Myr (first column), 400 Myr (second), 500 Myr (third) and 1 Gyr (fourth) with turbulent initial conditions. Here, we analyse the whole box in each simulation. The profiles of gas density (first row), temperature (second), entropy (third) and three-dimensional velocity dispersion (fourth) are shown. Solid lines show profiles from numerical simulations using RAMSES (blue), TPSH (yellow), PSPH (green) and MFM (red). The brown dashed line represents the KS01 model.

the spatial distribution of the hot bubble after it mixes with the ICM when employing different hydrodynamical solvers. Somewhat surprisingly however, the differences in the gas profiles are not very significant. While these results might imply that the choice of the hydrodynamical solvers is not the primary factor to explain differences in results obtained in different cosmological hydrodynamical simulations, we can only speculate here whether the differences we observed may be amplified if AGN feedback energy is injected repeatedly as the halo grows in mass. The amount of injected energy into the AGN bubble in our simulations, $\sim 10^{59}$ erg, was only $\sim 0.1\%$ of the total thermal energy of the ICM. As-

suming that the central super massive black hole, which is the engine of the AGN, has a mass of 10^9 $M_\odot$, the feedback energy over the timescale of our simulations, 1 Gyr, can be of order of $\sim 10^{62-63}$ erg if the AGN continues to be active (see e.g. Woo & Urry 2002). While this naïve estimation provides of course just an upper limit, the budget of feedback energy could be much greater than what we assumed and recursive injections of AGN bubbles are expected in a duty cycle behaviour of central fuel gas consumption and replenishment.

Even if the feedback energy is the same as assumed in this work, the impact of the bubbles may be greater if the ICM has a low-temperature core in the centre, i.e. in a cool-core cluster, so that the central gas is close to a runaway cooling instability. We will revisit this aspect in future work.

Last but not least, additional physical processes that this study does not take into account, such as magnetic fields and cosmic rays, may alter the evolution of the AGN bubble and the thermodynamics galaxy clusters. In particular, one would expect that magnetic tension acts to suppress the disruption and mixing of buoyantly rising bubbles. We will investigate the interactions between the AGN bubble and ICM using idealised MHD simulations of several kinds of hydrodynamical solvers in the subsequent paper (Biernacki et al., in prep.).

ACKNOWLEDGEMENTS

We would like to thank Arif Babul, Alessandro Lupi, Ewald Puchwein, and Joakim Rosdahl for stimulating conversations. We also thank Daisuke Nagai for his careful reading of the draft and providing insightful comments. This work heavily relied on the GIZMO (Hopkins 2015) and RAMSES (Teyssier 2002) codes and PYNBODY package (Pontzen et al. 2013). We would like to thank the authors for their efforts. GO and OH acknowledge funding from the European Research Council (ERC) under the European Union's Horizon 2020 research and innovation programme (grant agreement No. 679145, project 'COSMO-SIMS').

REFERENCES

Abel T., 2011, MNRAS, 413, 271
Agertz O., et al., 2007, MNRAS, 380, 963
Barnes J., Hut P., 1986, Nature, 324, 446
Barnes D. J., et al., 2017a, preprint, (arXiv:1710.08420)
Barnes D. J., et al., 2017b, MNRAS, 471, 1088
Battaglia N., Bond J. R., Pfrommer C., Sievers J. L., 2013, ApJ, 777, 123
Bîrzan L., Rafferty D. A., McNamara B. R., Wise M. W., Nulsen P. E. J., 2004, ApJ, 607, 800
Booth C. M., Schaye J., 2009, MNRAS, 398, 53
Brüggen M., Kaiser C. R., 2002, Nature, 418, 301
Cavagnolo K. W., McNamara B. R., Nulsen P. E. J., Carilli C. L., Jones C., Bîrzan L., 2010, ApJ, 720, 1066
Churazov E., Brüggen M., Kaiser C. R., Böhringer H., Forman W., 2001, ApJ, 554, 261
Cowie L. L., Binney J., 1977, ApJ, 215, 723
Dennis T. J., Chandran B. D. G., 2005, ApJ, 622, 205
Di Matteo T., Springel V., Hernquist L., 2005, Nature, 433, 604
Di Matteo T., Khandai N., DeGraf C., Feng Y., Croft R. A. C., Lopez J., Springel V., 2012, ApJ, 745, L29
Dolag K., Komatsu E., Sunyaev R., 2016, MNRAS, 463, 1797
Dong R., Stone J. M., 2009, ApJ, 704, 1309
Dong R., Rasmussen J., Mulchaey J. S., 2010, ApJ, 712, 883
Dubois Y., Peirani S., Pichon C., Devriendt J., Gavazzi R., Welker C., Volonteri M., 2016, MNRAS, 463, 3948
Duffell P. C., MacFadyen A. I., 2011, ApJS, 197, 15
Dunn R. J. H., Fabian A. C., Taylor G. B., 2005, MNRAS, 364, 1343
Dursi L. J., Pfrommer C., 2008, ApJ, 677, 993
Eckert D., Gaspari M., Vazza F., Gastaldello F., Tramacere A., Zimmer S., Ettori S., Paltani S., 2017, ApJ, 843, L29
Evrard A. E., 1997, MNRAS, 292, 289
Fabian A. C., 1994, ARA&A, 32, 277
Fabian A. C., 2012, ARA&A, 50, 455
Fabian A. C., Nulsen P. E. J., 1977, MNRAS, 180, 479
Fabian A. C., et al., 2000, MNRAS, 318, L65
Forman W., et al., 2007, ApJ, 665, 1057
Frenk C. S., et al., 1999, ApJ, 525, 554
Gaburov E., Johansen A., Levin Y., 2012, ApJ, 758, 103
Gaspari M., Melioli C., Brighenti F., D'Ercole A., 2011, MNRAS, 411, 349
Gingold R. A., Monaghan J. J., 1977, MNRAS, 181, 375
Gitti M., Feretti L., Schindler S., 2006, A&A, 448, 853
Godfrey L. E. H., Shabala S. S., 2013, ApJ, 767, 12
Guo F., Mathews W. G., 2011, ApJ, 728, 121
Hahn O., Martizzi D., Wu H.-Y., Evrard A. E., Teyssier R., Wechsler R. H., 2017, MNRAS, 470, 166
Hitomi Collaboration et al., 2016, Nature, 535, 117
Hopkins P. F., 2013, MNRAS, 428, 2840
Hopkins P. F., 2015, MNRAS, 450, 53
Hurier G., Angulo R. E., 2017, preprint, (arXiv:1711.06029)
Inutsuka S.-I., 2002, Journal of Computational Physics, 179, 238
Kawata D., Gibson B. K., 2005, MNRAS, 358, L16
Komatsu E., Seljak U., 2001, MNRAS, 327, 1353
Komatsu E., et al., 2011, ApJS, 192, 18
Kravtsov A. V., Borgani S., 2012, ARA&A, 50, 353
Landau L. D., Lifshitz E. M., 1959, Fluid mechanics. Oxford: Pergamon Press
Lanz L., Ogle P. M., Evans D., Appleton P. N., Guillard P., Emonts B., 2015, ApJ, 801, 17
Lau E. T., Kravtsov A. V., Nagai D., 2009, ApJ, 705, 1129
Lau E. T., Gaspari M., Nagai D., Coppi P., 2017, ApJ, 849, 54
Le Brun A. M. C., McCarthy I. G., Schaye J., Ponman T. J., 2014, MNRAS, 441, 1270
Lea S. M., Silk J., Kellogg E., Murray S., 1973, ApJ, 184, L105
Lucy L. B., 1977, AJ, 82, 1013
Mantz A. B., Allen S. W., Morris R. G., Rapetti D. A., Applegate D. E., Kelly P. L., von der Linden A., Schmidt R. W., 2014, MNRAS, 440, 2077
Martizzi D., Hahn O., Wu H.-Y., Evrard A. E., Teyssier R., Wechsler R. H., 2016, MNRAS, 459, 4408
Mathews W. G., Bregman J. N., 1978, ApJ, 224, 308
McCarthy I. G., et al., 2010, MNRAS, 406, 822
McNamara B. R., Nulsen P. E. J., 2007, ARA&A, 45, 117
McNamara B. R., et al., 2001, ApJ, 562, L149
Meece G. R., Voit G. M., O'Shea B. W., 2017, ApJ, 841, 133
Mingo B., Hardcastle M. J., Croston J. H., Evans D. A., Kharb P., Kraft R. P., Lenc E., 2012, ApJ, 758, 95
Miniati F., 2014, ApJ, 782, 21
Mitchell N. L., McCarthy I. G., Bower R. G., Theuns T., Crain R. A., 2009, MNRAS, 395, 180
Mo H., van den Bosch F. C., White S., 2010, Galaxy Formation and Evolution
Monaghan J. J., 1992, ARA&A, 30, 543
Monaghan J., 2012, Annual Review of Fluid Mechanics, 44, 323
Nagai D., Kravtsov A. V., Vikhlinin A., 2007, ApJ, 668, 1
Navarro J. F., Frenk C. S., White S. D. M., 1997, ApJ, 490, 493

Nelson K., Lau E. T., Nagai D., Rudd D. H., Yu L., 2014, ApJ, 782, 107
Nemmen R. S., Georganopoulos M., Guiriec S., Meyer E. T., Gehrels N., Sambruna R. M., 2012, Science, 338, 1445
Ohto A., Kawano N., Fukazawa Y., 2003, PASJ, 55, 819
Okamoto T., Jenkins A., Eke V. R., Quilis V., Frenk C. S., 2003, MNRAS, 345, 429
Okamoto T., Nemmen R. S., Bower R. G., 2008, MNRAS, 385, 161
Panagoulia E. K., Fabian A. C., Sanders J. S., Hlavacek-Larrondo J., 2014, MNRAS, 444, 1236
Perucho M., Martí J.-M., Quilis V., Ricciardelli E., 2014, MNRAS, 445, 1462
Planck Collaboration et al., 2016, A&A, 594, A13
Planelles S., Borgani S., Fabjan D., Killedar M., Murante G., Granato G. L., Ragone-Figueroa C., Dolag K., 2014, MNRAS, 438, 195
Pontzen A., Roškar R., Stinson G. S., Woods R., Reed D. M., Coles J., Quinn T. R., 2013, pynbody: Astrophysics Simulation Analysis for Python
Power C., Read J. I., Hobbs A., 2014, MNRAS, 440, 3243
Pratt G. W., et al., 2010, A&A, 511, A85
Price D. J., 2012, Journal of Computational Physics, 231, 759
Rasia E., et al., 2015, ApJ, 813, L17
Read J. I., Hayfield T., Agertz O., 2010, MNRAS, 405, 1513
Reynolds C. S., McKernan B., Fabian A. C., Stone J. M., Vernaleo J. C., 2005, MNRAS, 357, 242
Reynolds C. S., Balbus S. A., Schekochihin A. A., 2015, ApJ, 815, 41
Ritchie B. W., Thomas P. A., 2001, MNRAS, 323, 743
Robinson K., et al., 2004, ApJ, 601, 621
Roediger E., Brüggen M., Rebusco P., Böhringer H., Churazov E., 2007, MNRAS, 375, 15
Rosswog S., 2009, New Astron. Rev., 53, 78
Saitoh T. R., Makino J., 2013, ApJ, 768, 44
Sanders J. S., Fabian A. C., Taylor G. B., 2009, MNRAS, 393, 71
Sanderson A. J. R., Finoguenov A., Mohr J. J., 2005, ApJ, 630, 191
Schaller M., Dalla Vecchia C., Schaye J., Bower R. G., Theuns T., Crain R. A., Furlong M., McCarthy I. G., 2015, MNRAS, 454, 2277
Schuecker P., Finoguenov A., Miniati F., Böhringer H., Briel U. G., 2004, A&A, 426, 387
Schwarzschild K., 1906, Nachrichten von der Gesellschaft der Wissenschaften zu Göttingen, Mathematisch-Physikalische Klasse, 1906, 41
Sembolini F., et al., 2016, MNRAS, 459, 2973
Shurkin K., Dunn R. J. H., Gentile G., Taylor G. B., Allen S. W., 2008, MNRAS, 383, 923
Sijacki D., Springel V., 2006, MNRAS, 366, 397
Sijacki D., Springel V., Di Matteo T., Hernquist L., 2007, MNRAS, 380, 877
Springel V., 2010a, ARA&A, 48, 391
Springel V., 2010b, MNRAS, 401, 791
Steinborn L. K., Dolag K., Hirschmann M., Prieto M. A., Remus R.-S., 2015, MNRAS, 448, 1504
Sutherland R. S., Bicknell G. V., 2007, ApJS, 173, 37
Teyssier R., 2002, A&A, 385, 337
Teyssier R., Moore B., Martizzi D., Dubois Y., Mayer L., 2011, MNRAS, 414, 195
Vazza F., Gheller C., Brunetti G., 2010, A&A, 513, A32
Vernaleo J. C., Reynolds C. S., 2006, ApJ, 645, 83
Vogelsberger M., Genel S., Sijacki D., Torrey P., Springel V., Hernquist L., 2013, MNRAS, 436, 3031
Voit G. M., Meece G., Li Y., O'Shea B. W., Bryan G. L., Donahue M., 2017, ApJ, 845, 80
Wadsley J. W., Veeravalli G., Couchman H. M. P., 2008, MNRAS, 387, 427
Wagner A. Y., Bicknell G. V., Umemura M., 2012, ApJ, 757, 136
Wiersma R. P. C., Schaye J., Theuns T., 2011, MNRAS, 415, 353
Woo J.-H., Urry C. M., 2002, ApJ, 579, 530
Zhuravleva I., et al., 2014, Nature, 515, 85
ZuHone J., Miller E. D., Bulbul E., Zhuravleva I., 2017, preprint, (arXiv:1708.07206)
van Leer B., 1979, Journal of Computational Physics, 32, 101

APPENDIX A: A SPHERICALLY SYMMETRIC 1D MUSCL SOLVER

In this appendix, we briefly discuss our implementation of a one-dimensional, spherically symmetric hydrodynamics solver which we use to validate the results obtained with the three-dimensional simulation codes.

A1 Governing equations and numerical implementation

The equations of ideal hydrodynamics in conservative form and under spherical symmetry take the form

$$\frac{\partial \rho}{\partial t} + \frac{\partial (S\rho u)}{\partial V} = 0 \tag{A1}$$

$$\frac{\partial \rho u}{\partial t} + \frac{\partial \left(S(\rho u^2 + P)\right)}{\partial V} = -\frac{2P}{r} - \frac{\partial \phi}{\partial r} \tag{A2}$$

$$\frac{\partial \rho e_{\rm tot}}{\partial t} + \frac{\partial (S\rho h_{\rm tot} u)}{\partial V} = 0, \tag{A3}$$

where ρ is the density, u is the radial fluid velocity, $e_{\rm tot}$ the total specific energy, $h_{\rm tot}$ the total specific enthalpy, ϕ the gravitational potential, and S is the surface area, i.e. $S = 4\pi r^2$, at radius r. These equations are straightforwardly implemented into a standard 1D MUSCL solver (van Leer 1979), where only the geometric factors need to be inserted along with the source term $2P/r$. For time integration, we use a second order predictor-corrector scheme, just as RAMSES, where the predicted step is calculated using the primitive equations, then an approximate Riemann solver (we use HLL) is called to compute the Riemann fluxes at the cell interfaces. In an equivalent way, the source terms are advanced by a half time step using the old, and by another half step using the new solution after updating with fluxes.

A2 Validation of the 1D solver

We validate our simple one dimensional solver using the Sedov-Taylor point explosion problem, for which the self-similar analytic solution is known (e.g. Landau & Lifshitz 1959). The numerical solution, in dimensionless units, at time $t = 0.5$ for an explosion with initial energy $E = 1$, expanding into a background of density $\rho = 1$, and assuming a polytropic equation of state with exponent $\gamma = 5/3$, is shown for various resolutions in comparison to the analytic result in Fig. A1. We adopted a simulation domain of unit radius, so that the finite volume shells at a resolution of N points have a thickness of $\Delta r = N^{-1}$. The initial energy is inserted in the single innermost shell. We note that at all resolutions the shock has a thickness of ~ 2 shells.

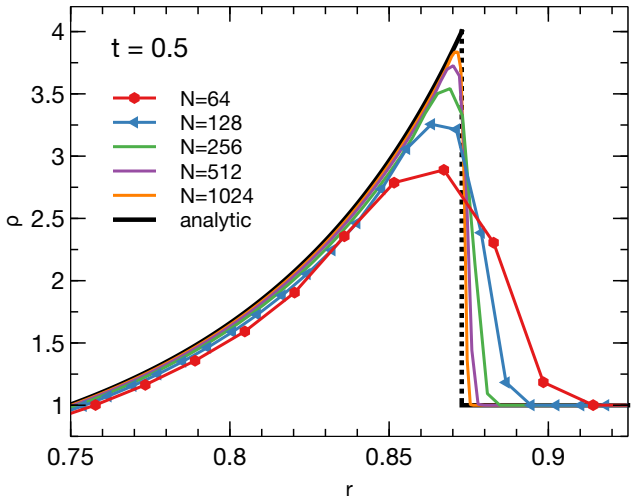

Figure A1. Convergence of the numerical solution to the Sedov-Taylor blast wave problem with increasing resolution for N = 64, 128, 256, 512 and 1024 grid points using our spherical 1D MUSCL scheme. We show results for the dimensionless density ρ at $t = 0.5$ for a region around the shock front (which is located at $r \simeq 0.873$).

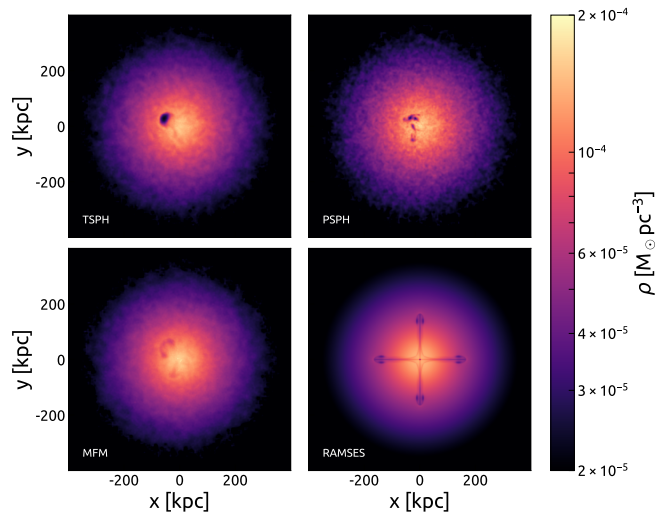

Figure B1. Slices through density distribution for TSPH (top left), PSPH (top right), MFM (bottom left) and RAMSES (bottom right) after 500 Myr of evolution with the central bubble. Each simulation is initialised in the same way - density and temperature follow KS01 and we artificially raise the temperature of fluid elements in the central sphere with a radius of 10 kpc to 10^9 K.

APPENDIX B: DENSITY SLICES FROM THE RUNS OF A CENTRAL BUBBLE

In this appendix, we present the slices of gas density in the runs with the central bubble. Fig. B1 shows the snapshot at $t = 500$ Myr. The bubble rises due to the Poisson noise in the initial condition of the simulations using GIZMO; this breaks the symmetry of the system. The bubble is very pronounced in the TSPH run (upper left) because the growth of the KHI is suppressed by the spurious tension on the bubble surface. In the PSPH (upper right) and MFM (lower left) runs, the bubble is dissolved the KHI. Because of the symmetry and absence of the Poisson noise a cross structure is formed in the RAMSES run (lower right).

APPENDIX C: RESOLUTION EFFECTS

We study how the results depend on the resolution of simulations. Fig. C1 compares simulation results varying the resolution. The left four panels are the density slices from simulations with the high resolution we adopt as the standard level and the right four are those from the runs with a degraded resolution level. The RAMSES simulations have similar numbers of leaf cells to the number of particles in the GIZMO simulations in each resolution level. The overall structures, e.g. direction to which the bubble is rising and position of the bubble, are well captured in the both resolution levels. However, one would find the differences between the two levels of resolution on the small scale, e.g. number of fragmented smaller bubbles and separation between them. In spite of the resolution dependence, our conclusion is not changed because the differences among the hydrodynamical solvers are more significant.

This paper has been typeset from a TEX/LATEX file prepared by the author.

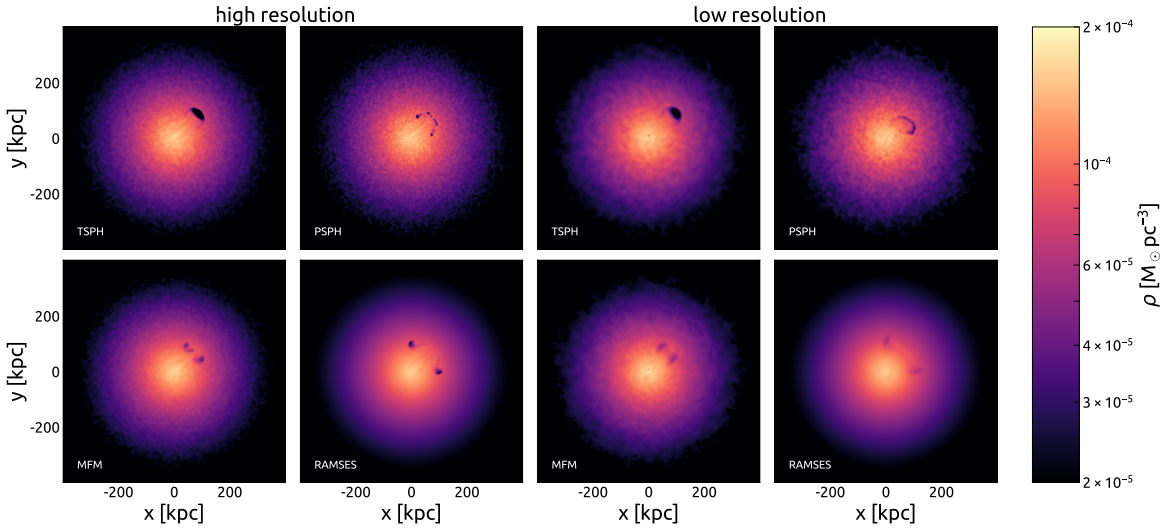

Figure C1. Resolution test. The left four panels show the density slices at $t = 500$ Myr obtained from simulations with the high resolution we adopt as the standard level (64 million particles in the GIZMO runs and `levelmax`=11 in the RAMSES run) and the right four show those in runs with a degraded resolution (8 million particles in the GIZMO runs and `levelmax`=9 in the RAMSES run). A shifted hot bubble is initially set and the turbulent velocity field is *not* introduced in all runs (for details see Subsection 4.3). In each group of panels, the results of simulations using TSPH, PSPH, MFM and RAMSES are illustrated in the upper left, upper right, lower left and lower right panels, respectively.